

**Deep-inelastic multinucleon transfer processes in the  $^{16}\text{O} + ^{27}\text{Al}$  reaction**

B. J. Roy,<sup>1,2,\*</sup> Y. Sawant,<sup>1</sup> P. Patwari,<sup>1</sup> S. Santra,<sup>1,2</sup> A. Pal,<sup>1,2</sup> A. Kundu,<sup>1,2</sup> D. Chattopadhyay,<sup>1,2</sup> V. Jha,<sup>1</sup> S. K. Pandit,<sup>1,2</sup> V. V. Parkar,<sup>1,2</sup> K. Ramachandran,<sup>1</sup> K. Mahata,<sup>1,2</sup> B. K. Nayak,<sup>1,2</sup> A. Saxena,<sup>1,2</sup> S. Kailas,<sup>1,2</sup> T. N. Nag,<sup>3</sup> R. N. Sahoo,<sup>4</sup> P. P. Singh,<sup>4</sup> and K. Sekizawa<sup>5,†</sup>

<sup>1</sup>*Nuclear Physics Division, Bhabha Atomic Research Centre, Mumbai 400 085, India*

<sup>2</sup>*Homi Bhabha National Institute, Anushakti Nagar, Mumbai 400 094, India*

<sup>3</sup>*Radio Chemistry Division, Bhabha Atomic Research Centre, Mumbai 400 085, India*

<sup>4</sup>*Department of Physics, Indian Institute of Technology Ropar, Rupnagar, Punjab 140 001, India*

<sup>5</sup>*Faculty of Physics, Warsaw University of Technology, Ulca Koszykowa 75, 00-662 Warsaw, Poland*



(Received 14 July 2017; revised manuscript received 26 January 2018; published 7 March 2018)

The reaction mechanism of deep-inelastic multinucleon transfer processes in the  $^{16}\text{O} + ^{27}\text{Al}$  reaction at an incident  $^{16}\text{O}$  energy ( $E_{\text{lab}} = 134$  MeV) substantially above the Coulomb barrier has been studied both experimentally and theoretically. Elastic-scattering angular distribution, total kinetic energy loss spectra, and angular distributions for various transfer channels have been measured. The  $Q$ -value- and angle-integrated isotope production cross sections have been deduced. To obtain deeper insight into the underlying reaction mechanism, we have carried out a detailed analysis based on the time-dependent Hartree-Fock (TDHF) theory. A recently developed method, TDHF+GEMINI, has been applied to evaluate production cross sections for secondary products. From a comparison between the experimental and theoretical cross sections, we find that the theory qualitatively reproduces the experimental data. Significant effects of secondary light-particle emissions are demonstrated. Possible interplay among fusion-fission, deep-inelastic, multinucleon transfer, and particle evaporation processes is discussed.

DOI: [10.1103/PhysRevC.97.034603](https://doi.org/10.1103/PhysRevC.97.034603)

**I. INTRODUCTION**

The mechanism of deep-inelastic processes which arise in an intermediate regime between the direct and the compound-nucleus reactions is notably complicated and has been a subject of extensive studies for a long time both experimentally and theoretically [1]. While it offers a precious opportunity to seek dissipation and equilibration mechanisms in complex nuclear many-body systems, clear-cut distinction between deep-inelastic and fusion-fission processes is particularly difficult to draw. The complexity even increases for light systems, due to a strong overlap between mass distributions of the fragments from different origins. In this paper, we report on reaction mechanism studies of deep-inelastic collisions in one such light system, the  $^{16}\text{O} + ^{27}\text{Al}$  reaction.

The quest for understanding the reaction mechanism with the  $^{16}\text{O} + ^{27}\text{Al}$  reaction started as early as 1959 [2]. Since then, along with continuous development of experimental techniques, numerous measurements were carried out for this system to identify, e.g., interplay between incomplete fusion and projectile breakup processes [3–10] and the mechanism of complete fusion [11–18]. Measurements for deep-inelastic and transfer processes were also performed [19–32]. Recently, the

elastic scattering of  $^{16}\text{O} + ^{27}\text{Al}$  at 100 MeV was also studied in the context of nuclear rainbow detection [33–36] that was predicted theoretically in Ref. [37].

In detailed studies of the  $^{16}\text{O} + ^{27}\text{Al}$  reaction at  $E_{\text{lab}} = 88$  MeV [23] and 90 and 100 MeV [22], it was observed that although the system is very light, the overall features of the reaction products are very similar to much heavier projectile-target combinations at higher collision energies [38–40]. It indicates that deep-inelastic transfer processes dominate the reaction and the reaction mechanism evolves gradually from quasielastic to deep-inelastic and to complete fusion. In going from  $E_{\text{lab}} = 90$  to 100 MeV, it was observed that the deep-inelastic cross section increases significantly. In another work, the authors of Ref. [21] concluded, based on the study of energy dependence of  $\gamma$ -ray yields, that up to at least  $E_{\text{lab}} = 165$  MeV the deep-inelastic transfer reactions will be the primary mechanism and any contribution from the fusion-fission is probably a small fraction of the total reaction cross section, though it was indirect evidence. Contrary to this, a later study of the same system at  $E_{\text{lab}} = 116$  MeV showed different results [30]. In that work, from the study of fragment emission spectra and using a simple two-Gaussian fitting procedure, the authors deduced deep-inelastic and fusion-fission components separately. It was observed that the fusion-fission is rather competitive with the deep-inelastic process. They got the same conclusion from the analysis applied to a neighboring system,  $^{16}\text{O} + ^{28}\text{Si}$  [31].

Despite the considerable progress in this field, the reaction mechanism of deep-inelastic multinucleon transfer processes

\*bjroy@barc.gov.in, bidyutr2003@gmail.com

†Present address: Center for Transdisciplinary Research, Institute for Research Promotion, Niigata University, Niigata 950-2181, Japan; sekizawa@phys.sc.niigata-u.ac.jp

is not fully understood. A concept of deep-inelastic transfer reactions was conjectured in 1970 by Gridnev *et al.* [20] in terms of an orbiting picture of a dinuclear complex, where the surfaces of two colliding nuclei have considerable overlap forming a neck structure during the collision, and it rotates as a whole and evolves in time. The dinuclear system evolves toward equilibrium by exchanging nucleons and changing its shape, but it eventually splits into two fragments before the compound-nucleus formation. Such a classical picture of the dinuclear system formation was successful in explaining the overall features of experimental angular distributions and isotope production cross sections in various systems [41]. On the other hand, in such deep-inelastic processes, reaction products must be highly excited, which leads to secondary particle evaporation. These processes—transfer followed by evaporation—may contribute significantly to the final yields and have to be carefully taken into consideration. We should also note that the deep-inelastic heavy-ion transfer reactions, apart from their importance for spectroscopic studies of yrast excitations in nuclei that are not accessible in standard fusion evaporation processes employing stable nuclei [42], are recently considered to be an efficient way to produce and study neutron-rich heavy nuclei in the region of astrophysical interest [43–45].

In view of its importance and with a motivation to further understand the mechanism of the deep-inelastic multinucleon transfer reaction, we have carried out an experiment for the  $^{16}\text{O} + ^{27}\text{Al}$  reaction at  $E_{\text{lab}} = 134$  MeV, an incident energy significantly above the Coulomb barrier ( $E/V_B \simeq 5.3$ , where  $V_B$  is the phenomenological fusion barrier [46,47]). Elastic-scattering angular distribution, total kinetic energy loss (TKEL) spectra and angular distributions for various transfer channels have been measured. Employing a microscopic framework of the time-dependent Hartree-Fock (TDHF) theory and its recent extension, TDHF+GEMINI [48], we have theoretically examined the underlying reaction mechanism. The latter approach combines TDHF with a statistical de-excitation model, GEMINI++ [49], allowing the evaluation of production cross sections for secondary reaction products. From the present experimental data and detailed analysis based on the TDHF theory, we aim to elucidate the underlying reaction mechanism in the  $^{16}\text{O} + ^{27}\text{Al}$  reaction.

The paper is organized as follows. In Sec. II, we describe details of the measurement and present the experimental data. In Sec. III, the results of the TDHF calculations are given and the reaction dynamics are investigated. In Sec. IV, total isotope production cross sections obtained from the experiment and those from TDHF(+GEMINI) are compared. We summarize this work in Sec. V.

## II. EXPERIMENTAL DETAILS AND RESULTS

The experiment was performed with  $^{16}\text{O}$ -ion beam at an incident energy of  $E_{\text{lab}} = 134$  MeV obtained from the Pelletron-LINAC accelerator facility, Mumbai, India. The energy uncertainty of LINAC beam was  $\pm 0.5$  MeV. The target used was  $^{27}\text{Al}$  foil of thickness  $540 \mu\text{g}/\text{cm}^2$ . Reaction products were detected using six silicon surface barrier (SSB) detector telescopes in  $\Delta E$ - $E$  configuration mounted on two movable

arms inside the 1.5-m-diameter General Purpose Scattering Chamber in the LINAC beam hall. A typical thickness of  $\Delta E$  detectors was  $\approx 40 \mu\text{m}$ , while  $E$  detectors were about 1 mm thick. The relative solid angle between the telescopes was measured by taking data at overlapping angles. The angular resolution of the telescopes was less than  $1.4^\circ$ . Data were stored as two-dimensional  $\Delta E$ - $E$  spectra and a typical spectrum is presented in Fig. 1, showing a good charge and mass separation of the projectile-like fragments (PLFs). The reaction products were identified following the standard particle identification (PI) technique as described in our earlier study [50].

The elastic-scattering angular distribution has been measured and is shown in Fig. 2. The data are plotted along with statistical errors and in most of the cases the error bars are within the data symbol. The absolute cross section was obtained by measuring the target thickness and detector solid angle. Target thickness was measured by  $\alpha$ -energy loss method that introduces an error of about 2% in the absolute cross section. In addition, the error due to the solid angle measurement was  $\sim 1\%$ . The angular distribution has been analyzed using the optical-model search program SFRESCO [51]. A volume Woods-Saxon form is used for the real and imaginary parts of the potential. The optical-model potential parameters of the same system studied at an incident energy of 42 MeV [15] were used as starting parameters. The obtained best-fit potential

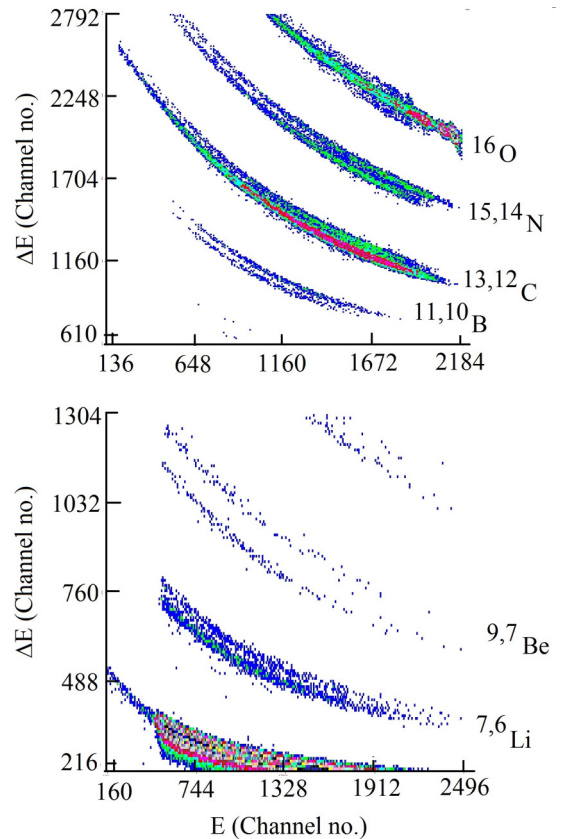


FIG. 1. A typical two-dimensional  $\Delta E$ - $E$  spectrum from  $^{27}\text{Al}(^{16}\text{O}, x)$  reactions at  $E_{\text{lab}} = 134$  MeV showing the various projectile-like fragments: (upper panel) oxygen, nitrogen, carbon, and boron isotopes; (lower panel) beryllium and lithium isotopes.

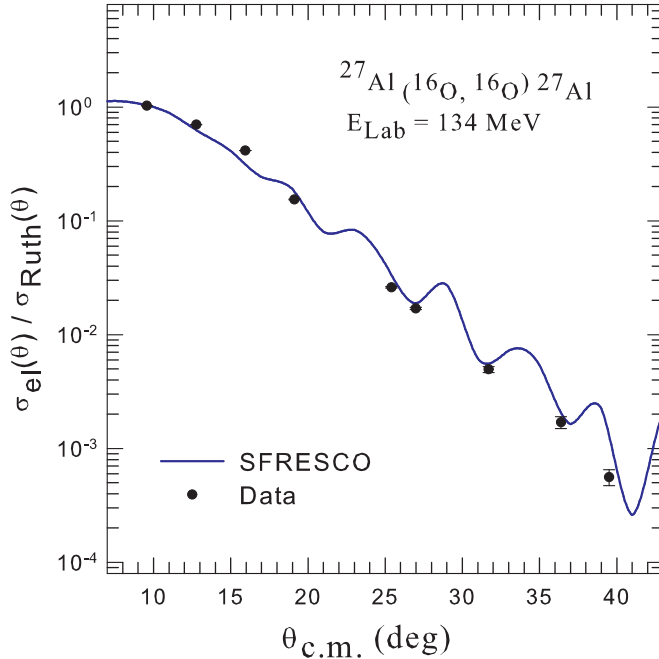


FIG. 2. The ratio of the elastic scattering to the Rutherford cross sections for the  $^{16}\text{O} + ^{27}\text{Al}$  reaction at  $E_{\text{lab}} = 134 \text{ MeV}$  plotted as a function of the scattering angle in the center-of-mass frame. Fitted result by the optical model calculation with the SFRESKO code [51] is shown by a blue solid curve. The potential parameters obtained from the fitting to the data are given in Table I.

parameters are listed in Table I. The cumulative reaction cross section,  $\sigma_{\text{R}}$ , is also shown in the table.

The  $Q$ -value spectra and angular distributions have been measured for reaction channels  $^{27}\text{Al}(^{16}\text{O}, x)$ , where  $x = ^{15,14}\text{N}$ ,  $^{13,12}\text{C}$ ,  $^{11,10}\text{B}$ ,  $^{9,7}\text{Be}$ , and  $^{7,6}\text{Li}$ , which correspond to a mass-number difference of up to  $\Delta A = A_{\text{PLF}} - A_{\text{Projectile}} = -10$ . It is important to mention that the pure neutron transfer channels, though visible at some of the angles, were not clearly separated from the  $^{16}\text{O}$  band in most of the cases and hence we could not study the TKEL spectra and angular distributions for those reactions. Also, for the spectra below lithium ( $Z = 3$ ), mass separation was not possible, and the energy spectrum for  $Z = 2$  reaction channel had significant foldback and overlaps

TABLE I. Potential parameters for the  $^{16}\text{O} + ^{27}\text{Al}$  system obtained from the optical-model analysis of the measured elastic-scattering cross section using the computer program SFRESKO [51]. The cumulative reaction cross section,  $\sigma_{\text{R}}$ , is also shown.

Potential parameters	$E_{\text{lab}} = 42 \text{ MeV}$ [15]	$E_{\text{lab}} = 134 \text{ MeV}$
$V_o$ (MeV)	60.0	67.46
$r_o$ (fm)	1.265	0.9
$a_o$ (fm)	0.472	0.55
$W$ (MeV)	9.0	10.0
$r_i$ (fm)	1.265	1.08
$a_i$ (fm)	0.472	0.71
$\sigma_{\text{R}}$	978.16 mb	1379.3 mb

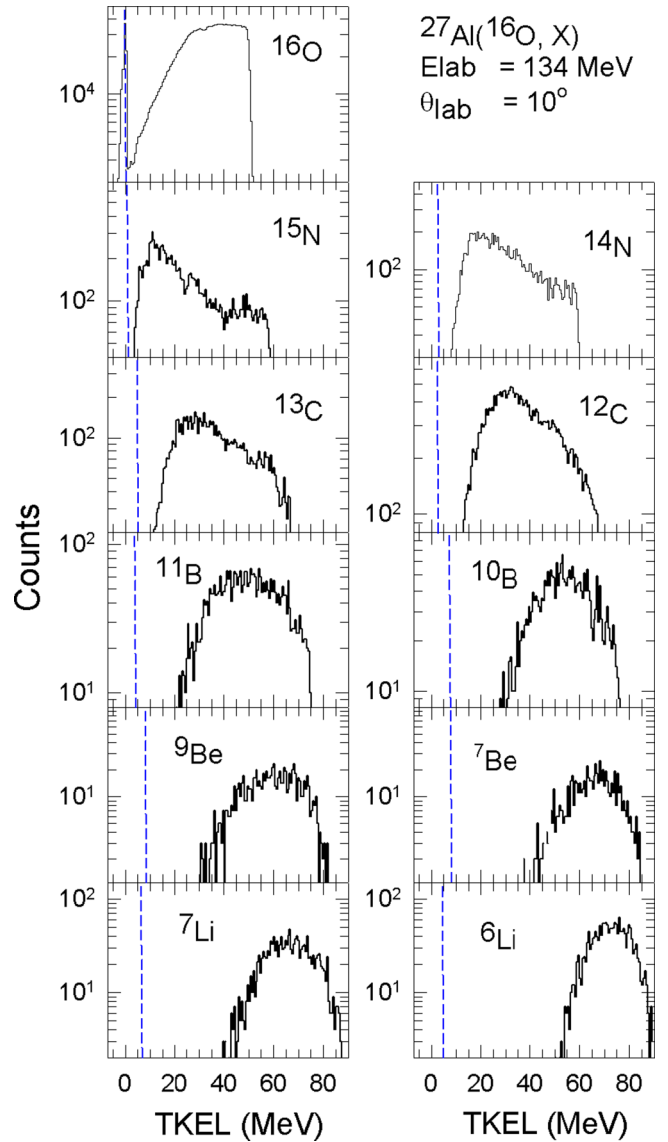


FIG. 3. Experimental total kinetic energy loss (TKEL) distributions (histogram plot) for various projectile-like fragments in the  $^{16}\text{O} + ^{27}\text{Al}$  reaction at  $E_{\text{lab}} = 134 \text{ MeV}$ , for a fixed scattering angle of  $\theta_{\text{lab}} = 10^\circ$  ( $\theta_{\text{c.m.}} = 15.9^\circ$ ). The blue vertical dashed lines indicate the position of ground-to-ground-state  $Q$  values.

with  $Z = 1$  channel. It was therefore not possible to extract the cross section for  $^4\text{He}$  ( $\alpha$ ) production.

The experimental TKEL spectra at  $\theta_{\text{lab}} = 10^\circ$  ( $\theta_{\text{c.m.}} = 15.9^\circ$ ) for various channels are shown in Fig. 3. The TKEL are derived assuming a pure binary process [52–55]. For the transfer reactions, as the number of transferred nucleons increases, there is a gradual shift of the centroid of energy-loss spectra toward the larger TKEL and reaches to as large as  $\sim 70 \text{ MeV}$  for the  $^{27}\text{Al}(^{16}\text{O}, ^6\text{Li})$  channel. We note that even for the inelastic channel without nucleon transfer ( $^{16}\text{O}, ^{16}\text{O}^*$ ), a substantial energy loss up to about  $50 \text{ MeV}$  has been observed (see the left top panel of Fig. 3). The sharp falloff above  $50 \text{ MeV}$  corresponds to the low-energy part of  $^{16}\text{O}$  that gets stopped in the  $\Delta E$  detector. Population of the bulk of events with

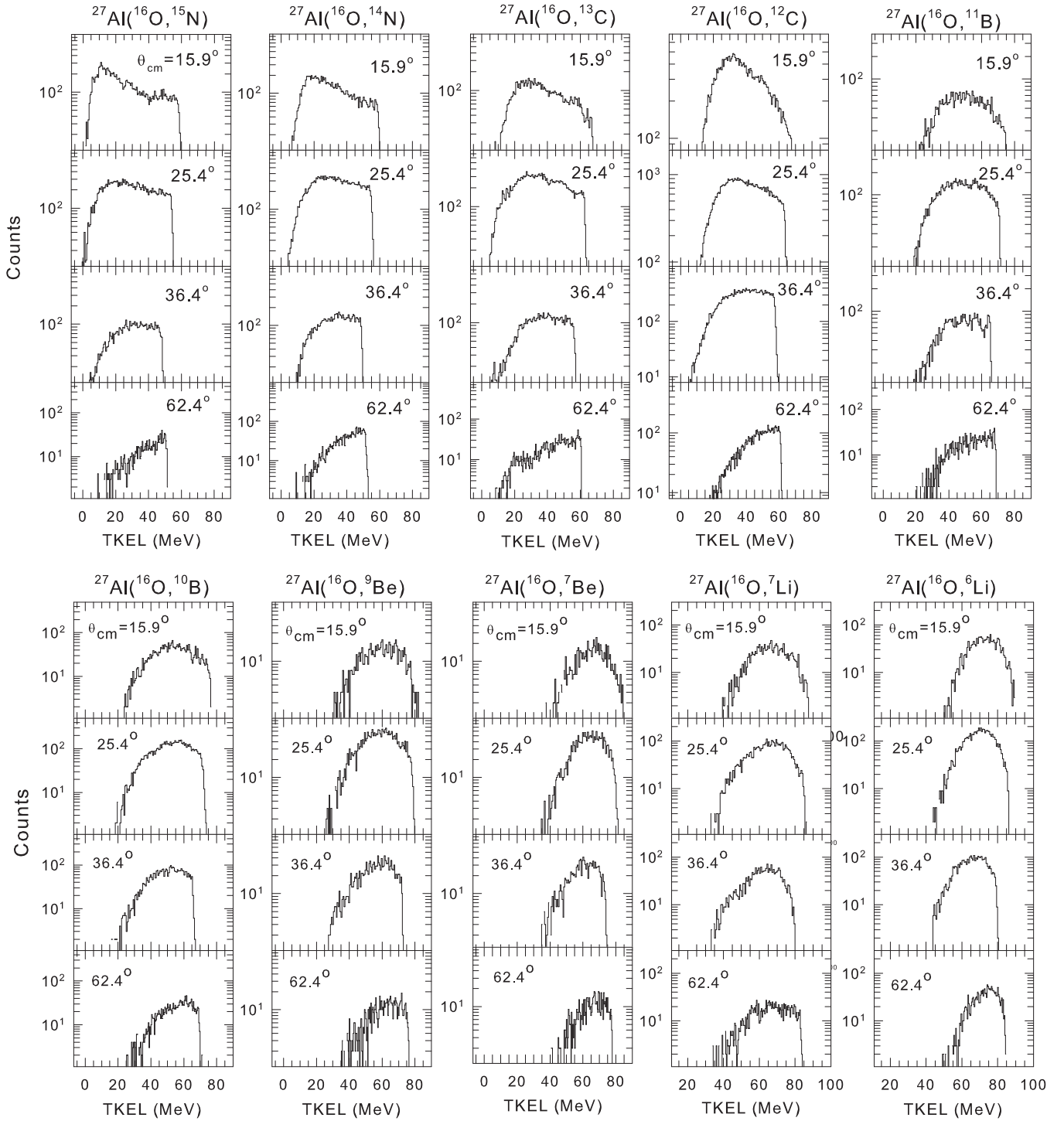


FIG. 4. The experimental total kinetic energy loss spectra of  $^{15}\text{N}$ ,  $^{14}\text{N}$ ,  $^{13}\text{C}$ ,  $^{12}\text{C}$ , and  $^{11}\text{B}$  (top row, from left to right) and  $^{10}\text{B}$ ,  $^9\text{Be}$ ,  $^7\text{Be}$ ,  $^7\text{Li}$ , and  $^6\text{Li}$  (bottom row, from left to right) reaction products from the  $^{16}\text{O} + ^{27}\text{Al}$  reaction at  $E_{\text{lab}} = 134$  MeV. Note that the vertical axis was adjusted case by case for better visibility. Note also that the data shown in the top row ( $\theta_{\text{c.m.}} = 15.9^\circ$ ) are the same data as shown in Fig. 3.

large energy losses (corresponds to higher excitation energy) may be associated with high density of excited states, which was observed in several other studies, e.g., in the  $^{27}\text{Al}(^{16}\text{O}, ^{16}\text{O}^*)$  inelastic scattering at 280 MeV [36] and in the  $^{27}\text{Al}(\alpha, \alpha')$  scattering [56,57]. The strong excitation in this region, as mentioned in those references, could be due to contributions from the isoscalar giant quadrupole resonance mode [57]

and octapole excitations [56] of  $^{27}\text{Al}$ . There could also be contributions from  $^{16}\text{O}$  particles originated from decay of excited ejectiles created in pickup reactions like  $^{17}\text{O}$ , decaying into  $^{16}\text{O} + n$  [36].

To get a better understanding of the reaction mechanism, the scattering angle dependence of the TKEL spectra has also been examined. In Fig. 4, we show the TKEL spectra of various

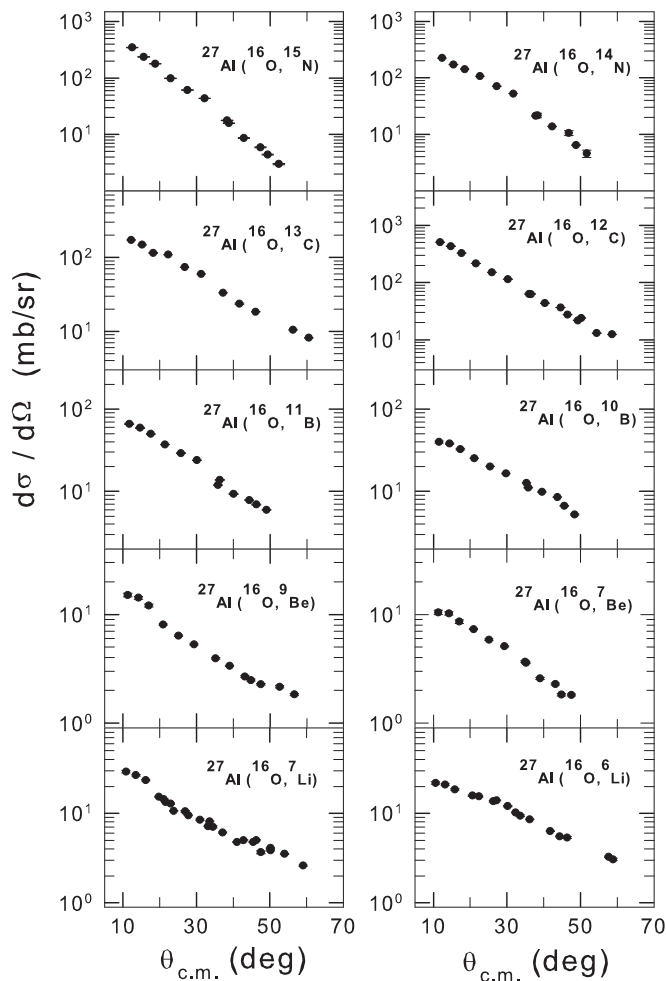


FIG. 5. The measured  $Q$ -value-integrated angular distributions for various channels in the  $^{16}\text{O} + ^{27}\text{Al}$  reaction at  $E_{\text{lab}} = 134$  MeV. The errors indicate the statistical error.

reaction products for several selected scattering angles,  $\theta_{\text{c.m.}} = 15.9^\circ, 25.4^\circ, 36.4^\circ,$  and  $62.4^\circ$ . By comparing the TKEL spectra of various transfer channels for each fixed scattering angle (on the same row), one can again see the gradual shift toward larger TKEL, as the number of transferred nucleons increases. For channels with relatively small number of transferred nucleons (i.e.,  $^{14,15}\text{N}$ ,  $^{12,13}\text{C}$ ), we find a clear angular dependence of the TKEL spectra. Namely, for those channels low-TKEL components dominate at forward angles, but the low-TKEL components decreases rapidly as the scattering angle increases. On the other hand, for processes with reaction products of  $^{10,11}\text{B}$ ,  $^{7,9}\text{Be}$ , and  $^{6,7}\text{Li}$ , we observe somewhat smaller angular dependence, always dominated by large-TKEL components. It may indicate that those reaction products are associated with deep-inelastic reactions and are affected substantially by secondary de-excitation processes.

The  $Q$ -value-integrated angular distributions for various reaction channels have been obtained by an appropriate selection of mass and charge of the reaction products and are shown in Fig. 5. The angular distributions are forward peaked, consistent with earlier studies for the same system at energies well

above the Coulomb barrier [22,23]. The strong forward-peaked nature of the multinucleon transfer angular distributions, in contrast to the bell-shaped angular distributions which are typical characteristic of quasielastic processes, is an indication of the increasing importance of nuclear effects and dissipative processes that occur at shorter internuclear distance [58].

The  $Q$ -value- and angle-integrated isotope production cross sections for various transfer processes have been obtained by fitting the angular distribution by an exponential function  $d\sigma/d\theta \propto \exp[-\alpha\theta]$  (as suggested in Refs. [59,60]) and integrating over whole angular range, 0 to  $180^\circ$ . The fitting procedure introduced an uncertainty of 9–13% in the final value of the cross section in most of the reaction channels except for  $^9\text{Be}$  and  $^{13}\text{C}$  for which a slightly larger error ( $\approx 16$ – $17\%$ ) was obtained. We note that we also tried a fitting with  $d\sigma/d\theta \propto \exp[-\alpha\theta]/\sin\theta$  (used in Ref. [23]), but the latter was giving somewhat poor fit in some of the reaction channels and resulted in large errors (more than 30% error in some cases). Therefore, we have decided to use the fit with the simple exponential function. The integrated cross sections are presented in Sec. IV (Fig. 11), where we compare the data with theoretical calculations.

### III. TDHF ANALYSIS

To gain deeper insight into the reaction mechanism, we have performed TDHF calculations for the  $^{16}\text{O} + ^{27}\text{Al}$  reaction. We used a parallel computational code developed by Sekizawa and Yabana [61]. The code has been tested and successfully applied for various systems [48,50,61–66]. The details of the calculations can be found in the references given above. Here we provide brief information relevant to the present analysis. Details of the TDHF theory and its application to nuclear dynamics can be found in Refs. [67–71].

In the TDHF approach, internal degrees of freedom are described microscopically from nucleonic degrees of freedom, whereas the collective motions of two colliding nuclei are described semiclassically through dynamics of a time-dependent mean-field potential generated by the interaction among all the nucleons. The theory can describe important features of the low-energy heavy-ion reaction, such as the Pauli principle among nucleons, shell effects, energy dissipations, nucleon exchanges, and shape evolution dynamics in the composite system formed in the course of the collision, on the same footing. The only input to the calculations is an effective nucleon-nucleon interaction (or an energy density functional, EDF), which is determined so as to reproduce known properties of finite nuclei and nuclear matter. Thus, in the TDHF approach, there is no adjustable (empirical) parameter specific to the reaction.

For the EDF, the Skyrme SLy5 parameter set [72] was used. Static Hartree-Fock (HF) calculations were performed in a cubic box with 24 fm on each side. The mesh spacing was set to 0.8 fm for both static and dynamic calculations. The HF ground state of  $^{16}\text{O}$  is of spherical shape, whereas that of  $^{27}\text{Al}$  turned out to be of a triaxial shape with  $\beta \simeq 0.27$  and  $\gamma \simeq 48^\circ$ . For the  $^{27}\text{Al}$  nucleus, a large oblate deformation is expected [73]. Since the deformation is quite large, TDHF calculations were performed taking three initial orientations of

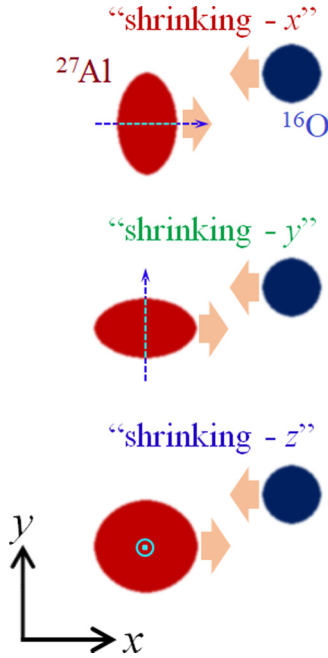


FIG. 6. A schematic illustration of the initial orientations of  $^{27}\text{Al}$  in the TDHF calculations. Red (blue) disk represents cross sections of the density of  $^{27}\text{Al}$  ( $^{16}\text{O}$ ) nucleus in the reaction plane ( $xy$  plane). The incident direction is indicated by thick arrows which are parallel to the  $x$  axis (at infinitely large distance), and the impact parameter vector is parallel to the  $y$  axis. By a blue dashed arrow or a circle attached to  $^{27}\text{Al}$ , the direction of shrinking is represented. This direction would correspond to the symmetry axis if  $^{27}\text{Al}$  were purely deformed in an oblate shape.

$^{27}\text{Al}$ . As the shape looks more or less like an oblate shape, those three orientations will be labeled according to the direction of “shrinking” of the total density, which would correspond to the symmetry axis if the nucleus were purely deformed in an oblate shape (see Fig. 6). In the TDHF calculations, we set the collision axis to the  $x$  direction and the impact parameter vector parallel to the  $y$  axis. Thus the reaction plane corresponds to the  $xy$  plane. A three-dimensional box of  $60\text{ fm} \times 52\text{ fm} \times 24\text{ fm}$  was used without symmetry restrictions. The initial separation distance between the projectile and target nuclei was set to  $24\text{ fm}$ . TDHF calculations were performed for an impact parameter range of  $[0, 12]$  (fm). The minimum impact parameter for binary reactions,  $b_{\text{min}}$ , inside which fusion reactions take place was searched by repeating TDHF calculations with an  $0.001\text{-fm}$  impact parameter step. The very small impact parameter step was chosen so as to capture a rapid change of the reaction dynamics in the vicinity of the fusion threshold. From the results, we find  $b_{\text{min}} = 7.025, 6.348, \text{ and } 6.899\text{ fm}$  for the shrinking  $x, y, \text{ and } z$  cases, respectively. Inside this impact parameter ( $b = 0, 1, \dots, 6, \text{ and } b_{\text{min}} - 0.001\text{ fm}$ ), fusion reactions were observed, where a mononuclear composite system persists in a compact shape within the simulation time of more than  $26\text{ zs}$  ( $1\text{ zs} = 10^{-21}\text{ s}$ ). In this context, we note that the fusion excitation function for the present system in the energy range  $E_{\text{lab}} = 25\text{--}200\text{ MeV}$  was studied in the past [74] within TDHF, where no fusion

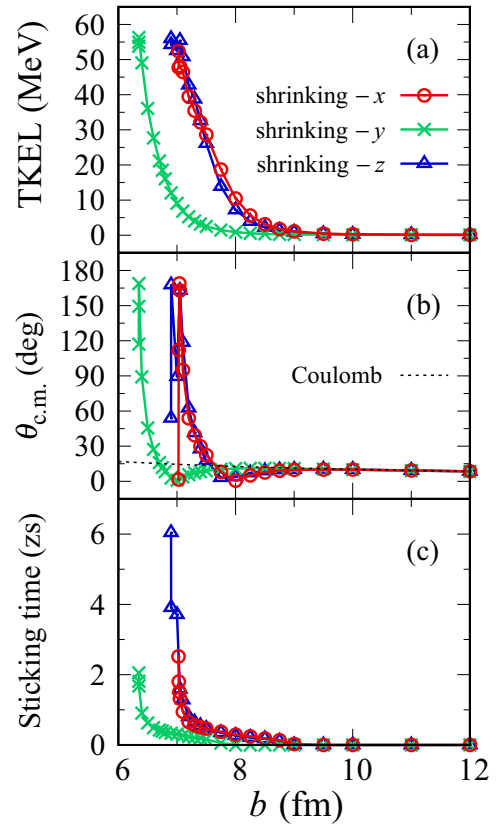


FIG. 7. Results of the TDHF calculations for the  $^{16}\text{O} + ^{27}\text{Al}$  reaction at  $E_{\text{lab}} = 134\text{ MeV}$ . (a) Total kinetic energy loss (TKEL), (b) scattering angle in the center-of-mass frame, and (c) sticking time are shown as a function of the impact parameter,  $b$ . In panel (b), the scattering angle for the Coulomb trajectory is indicated by a dotted curve. In panel (c), the sticking time is shown in zeptoseconds ( $1\text{ zs} = 10^{-21}\text{ s}$ ).

was observed at small impact parameters (the so-called fusion window) for  $E_{\text{lab}} > 100\text{ MeV}$  that might be due to the various approximations that were used in those calculations. Coming back to the present TDHF calculations, the time evolution for the binary reactions ( $b \geq b_{\text{min}}$ ) was continued until the relative distance between the reaction products reaches  $26\text{ fm}$ . Various reaction outcomes were then computed from TDHF wave functions after the collision with well-separated reaction products.

First, let us examine global features of the reaction dynamics. From the dynamics of the mean-field potential, average (most probable) reaction trajectories can be evaluated. We show TKEL in Fig. 7(a), the scattering angle in the center-of-mass frame in Fig. 7(b), and the sticking time in Fig. 7(c) as a function of the impact parameter. Red open circles, green crosses, and blue open triangles show the results associated with the different initial orientations of  $^{27}\text{Al}$ , corresponding to the shrinking  $x, y, \text{ and } z$  cases, respectively (cf. Fig. 6). Henceforth, the same colors and symbols will be used to indicate these orientations in the figures. In Fig. 7(b), the scattering angle for the Coulomb trajectory is indicated by a black dotted curve. The sticking time is the time duration in

which the lowest density between two colliding nuclei exceeds a critical value,  $\rho_c = 0.01 \text{ fm}^{-3}$ .

From the figure, we find that the global features of the reaction dynamics do not depend much on the initial orientations of  $^{27}\text{Al}$ . When the impact parameter is relatively large ( $b > 9 \text{ fm}$ ), TKEL is very small and the scattering angle coincides with the one for the Coulomb trajectory. As the impact parameter decreases ( $b < 9 \text{ fm}$ ), TKEL increases rapidly, reaching the maximum value of around 55 MeV. The maximum value of TKEL reasonably agrees with the experimental observation in Figs. 3 and 4. In this regime, the density of the colliding nuclei overlaps in the course of the collision, as can be seen as a gradual increase of the sticking time in Fig. 7(c), and, as a result, the scattering angle largely deviates from the Coulomb trajectory. We note that no nuclear rainbow is observed in TDHF, as all trajectories for  $b < b_{\min}$  resulted in fusion; the large scattering angles merely correspond to large negative deflection angles. Only a visible orientation dependence seen in Fig. 7 is a shift of the curves toward the smaller impact parameters (about 1 fm) in the shrinking y case (green crosses), as compared to the other cases. This difference can be simply understood from the collision geometry depicted in Fig. 6. Since we chose the impact parameter vector parallel to the y axis, the system requires smaller impact parameters in order to collide deeply in the shrinking y case. This explains the orientation dependence seen in Fig. 7. (A somewhat longer sticking time for  $b \approx b_{\min}$  in the shrinking z case will be discussed later.)

Combining the information of the TKEL and the scattering angle in Figs. 7(a) and 7(b), we make the so-called Wilczyński plot [75], which is shown in Fig. 8(a). We note that it has been considered that TDHF can reasonably capture main reaction dynamics in deep-inelastic collisions (i.e., the most probable trajectory in the Wilczyński plot) since the very early stage [76–80], which has been confirmed also in a recent experimental and theoretical study reported in Ref. [81]. The plot shows characteristic behavior for deep-inelastic reactions: a decrease of the scattering angle with larger TKE, followed by a rapid increase of the scattering angle accompanying large energy losses. At this collision energy substantially above the Coulomb barrier, a dinuclear system rotates a lot in the reaction plane and it finally reseparates. The dynamics result in appearance of the fragments in a wide angular range after the significant energy dissipation, indicating orbiting dynamics of the dinuclear system.

In contrast to the reaction dynamics shown in Figs. 7 and 8(a), we find that the fragment masses show noticeable orientation dependence. It can be clearly seen in Fig. 8(b), where we show the total kinetic energy versus mass distribution of the reaction products. For comparison, empirical values from the Viola systematics [82–84] are also shown by a gray solid curve. The two peaks at around  $A = 16$  and 27 correspond to the quasielastic peak for the PLF and the target-like fragment (TLF), respectively. From the figure, we see that the reaction products tend to be slightly mass asymmetric in the shrinking y case (green crosses). On the other hand, up to certain energy losses ( $\text{TKE} \approx 40$ ), the average fragment masses are nearly constant in the shrinking x and z cases. As the energy loss increases further ( $\text{TKE} \lesssim 40$ ), however, those two cases

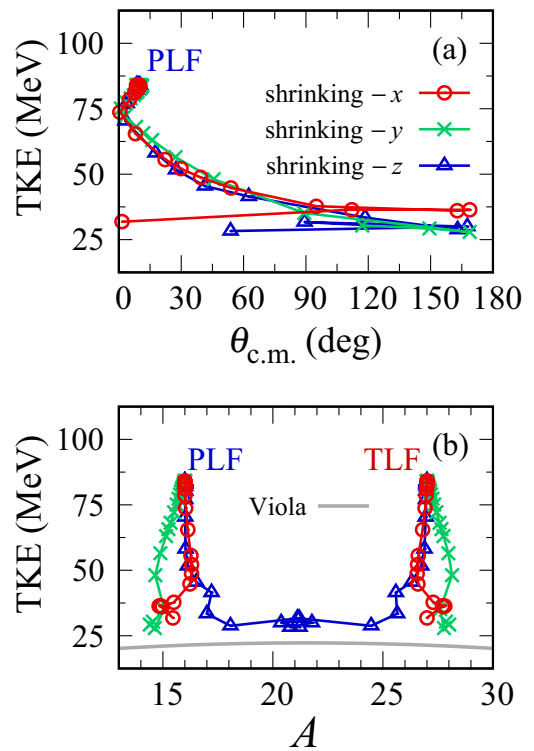


FIG. 8. (a) The Wilczyński plot and (b) the TKE-A distribution obtained from the TDHF calculations for the  $^{16}\text{O} + ^{27}\text{Al}$  reaction at  $E_{\text{lab}} = 134 \text{ MeV}$ .

deviate each other. Intriguingly, only in the shrinking z case (blue open triangles) does the composite system tend to evolve toward the mass symmetry. In this case, the reaction proceeds on the equatorial side of the oblatelike  $^{27}\text{Al}$  (cf. Fig. 6). We note that for all orientations TKE values become rather close to the Viola systematics, although not fully coincide. The behavior nicely mimics the one observed in heavy systems.

Average numbers of neutrons [Fig. 9(a)] and protons [Fig. 9(b)] of the PLF are shown as a function of the impact parameter. From the figure, we find some orientation dependence of the transfer processes. In the shrinking z case, we find that both neutrons and protons are transferred toward the same direction from  $^{27}\text{Al}$  to  $^{16}\text{O}$ , as the impact parameter decreases. The maximum values,  $N_{\text{PLF}} \approx 11$  and  $Z_{\text{PLF}} \approx 10.5$ , correspond to the symmetric division of the composite system, consistent with the observation in Fig. 8(b). On the other hand, in the shrinking y case, neutrons and protons are transferred toward the direction slightly increasing the mass asymmetry. The shrinking x case exhibits an intermediate behavior, as first few nucleons are transferred from  $^{27}\text{Al}$  to  $^{16}\text{O}$ , and then the direction changes, as the impact parameter decreases. The observed difference may be related to the properties of single-particle orbitals. In an oblate(-like) nucleus, single-particle orbitals tend to extend toward the equatorial side, which may prefer nucleon transfer from  $^{27}\text{Al}$  to  $^{16}\text{O}$ . While along the axis of shrinking, the orbitals tend not to extend, which may prefer transfer in the opposite direction. A similar trend was observed in our earlier study [50], where prolately deformed  $^{18}\text{O}$  induced transfer reactions were examined within TDHF. In Fig. 9(c),

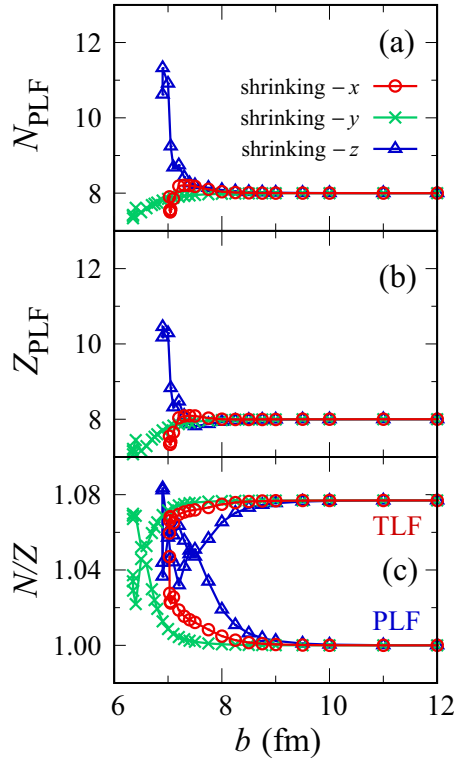


FIG. 9. Average numbers of neutrons (a) and protons (b) of the projectile-like fragment (PLF) in  $^{16}\text{O} + ^{27}\text{Al}$  reaction at  $E_{\text{lab}} = 134$  MeV are shown as a function of the impact parameter,  $b$ . In panel (c), the average  $N/Z$  ratios of the PLF and the targetlike fragment (TLF) are shown.

average  $N/Z$  ratios of the fragments are shown. Although the  $N/Z$  ratios are very close to each other before the collision, the reaction tends to proceed toward further charge equilibration. At small impact parameters close to the fusion threshold, the  $N/Z$  ratios fluctuate, because of the much longer sticking time and complex dynamics in the dinuclear system.

The results of the TDHF calculations indicate that certain mass symmetric fragments should emerge as a result of deeply inelastic reactions, which exhibit fusion-fission-like character, i.e., with fully damped kinetic energy and isotropic angular distribution. Although it was not possible in the present experimental setup to cover wider angular range and detect heavier PLFs and TLFs, it is nowadays routinely performed, especially for heavier systems (see, e.g., Refs. [81,85–88], and references therein). Detailed comparisons between experimental and theoretical data for the mass-angle correlation and the Wilczyński plot would provide us deeper understanding of the reaction dynamics.

To understand better the observed behavior, we show in Fig. 10 the time evolution of the density of the colliding nuclei for two representative cases: the shrinking  $y$  and  $z$  cases are shown in Figs. 10(a) and 10(b), respectively. Both cases correspond to the reaction at the minimum impact parameter for binary reactions,  $b_{\text{min}}$ . These two cases resulted in production of different nuclei as mentioned above: The average reaction product was  $Z_{\text{PLF}} \simeq 7.2$  and  $N_{\text{PLF}} \simeq 7.4$  for the shrinking  $y$  case, while it was  $Z_{\text{PLF}} \simeq$

10.2 and  $N_{\text{PLF}} \simeq 10.6$  for the shrinking  $z$  case. We shall now examine how the collision dynamics differ in those cases.

In the top row of Figs. 10(a) and 10(b), the initial stage of the reaction is displayed. As can be seen from the figure, two nuclei start colliding at around  $t = 0.6$  zs, then merge deeply due to the strong attractive interaction ( $t = 0.93$  zs). Because of the substantial angular momentum brought into the system, an elongated composite system is created ( $t = 1.27$  zs). At this stage, one can see that the system exhibits quite different shapes depending on the initial orientations of  $^{27}\text{Al}$  that makes subsequent dynamics so different. In the shrinking  $y$  case [Fig. 10(a)], the neck is rather thin, and it ruptures shortly within about 1 zs ( $t = 1.6$ – $2.67$  zs). Although the sticking time is relatively short, more than  $180^\circ$  rotation is achieved in the reaction plane. In contrast, in the shrinking  $z$  case [Fig. 10(b)], the elongated composite system exhibits a rather thick neck structure ( $t = 1.27$  zs), which persists for much longer time (about 5 zs). From the second row, each panel shows the composite system every after about  $90^\circ$  rotation in the reaction plane ( $t = 2.13$ – $5.6$  zs). From a careful look at the figure, we find that the system has rotated as large as  $720^\circ$ . It is interesting to observe that how the mass equilibration is achieved in such a light asymmetric system. By looking at the density, we find that the composite system shows rather complex shapes in the course of the collision. For instance, one may follow the smaller subsystem that was initially the  $^{16}\text{O}$  nucleus, e.g., the top part of the dinuclear system at  $t = 0.6$  zs in Fig. 10(b). As time evolves from  $t = 0.6$  to  $t = 2.67$  zs, the system rotates about  $360^\circ$ . However, as seen in the figure ( $t = 2.67$  zs), the subsystem (top part) that was smaller at the initial stage now looks larger than the other, indicating substantial nucleon exchanges from one nucleus to the other in the dinuclear system (see Supplemental Material [89] for movies of the reactions). Because of the nucleon exchanges and the long sticking time, the system achieved the mass equilibration in the shrinking  $z$  case. The present results indicate that deep-inelastic processes may substantially contribute to the generation of mass symmetric fragments in this reaction, which may be associated with zeptoseconds sticking time ( $\gtrsim 4$  zs, cf. Figs. 7 and 9) and perhaps originate from shrinking- $z$ -like collision geometries.

In the TDHF approach, it is not straightforward to evaluate angular distributions, due to the semiclassical nature of the collective motions. Nevertheless, the calculation can produce the total isotope production cross sections which is very useful information for understanding the reaction mechanism aspects. In the next section, we compare the TDHF results with the experimental data for the integrated isotope production cross sections.

#### IV. CROSS SECTION COMPARISON

As mentioned in Sec. II, we have deduced the  $Q$ -value- and angle-integrated cross sections for various transfer channels from the measured angular distributions (Fig. 5). In Fig. 11, we present the experimental data of the isotope production cross sections, which are represented by red filled circles. The horizontal axis is the neutron number of the PLFs. In each

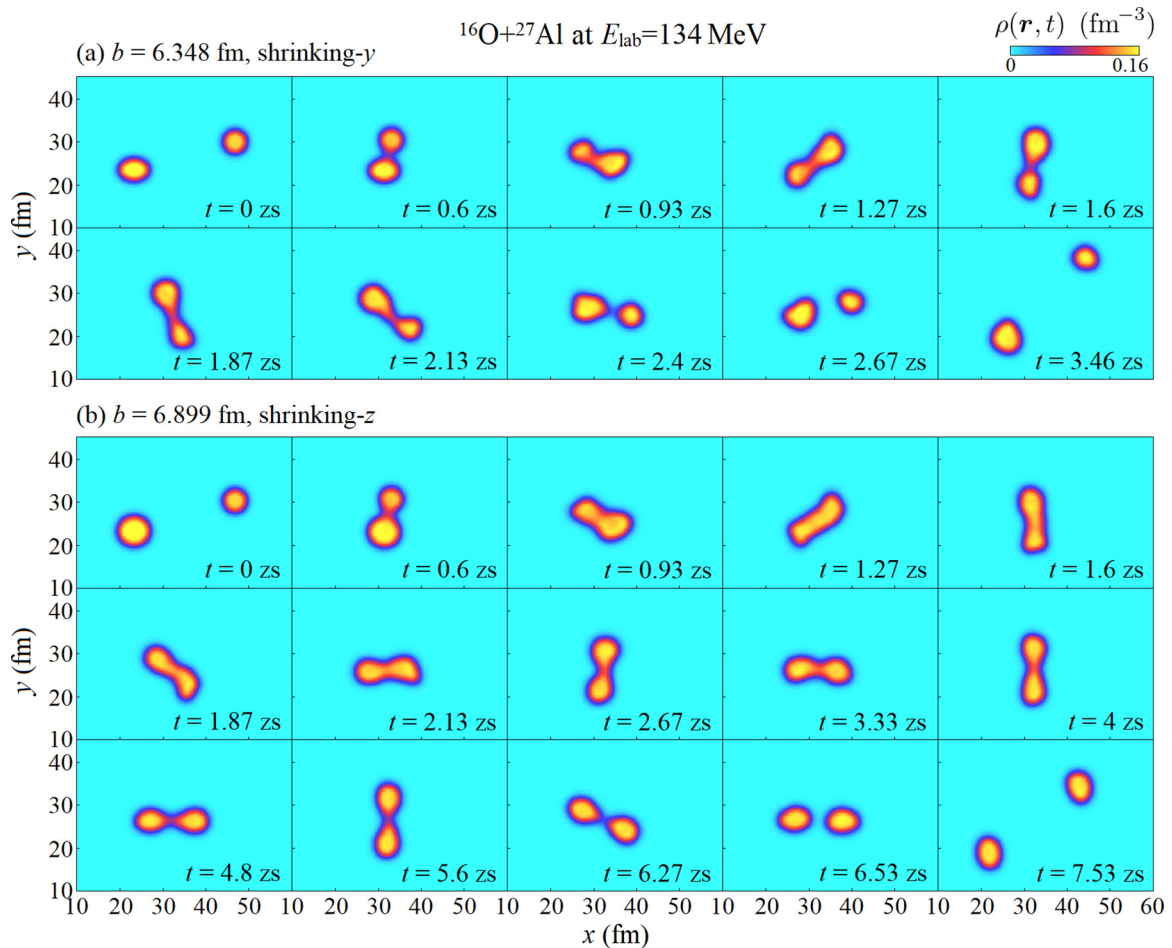


FIG. 10. Snapshots of the density of the colliding nuclei in the reaction plane at various times obtained from the TDHF calculations for the  $^{16}\text{O} + ^{27}\text{Al}$  reaction at  $E_{\text{lab}} = 134$  MeV. In upper panels (a), dynamics for the shrinking  $y$  case are shown, while those for the shrinking  $z$  case are shown in lower panels (b). In each panel, the elapsed time is indicated in zeptoseconds ( $1 \text{ zs} = 10^{-21} \text{ s}$ ). It is to mention that the whole simulation box ( $60 \text{ fm} \times 52 \text{ fm}$ ) is not shown in the figure.

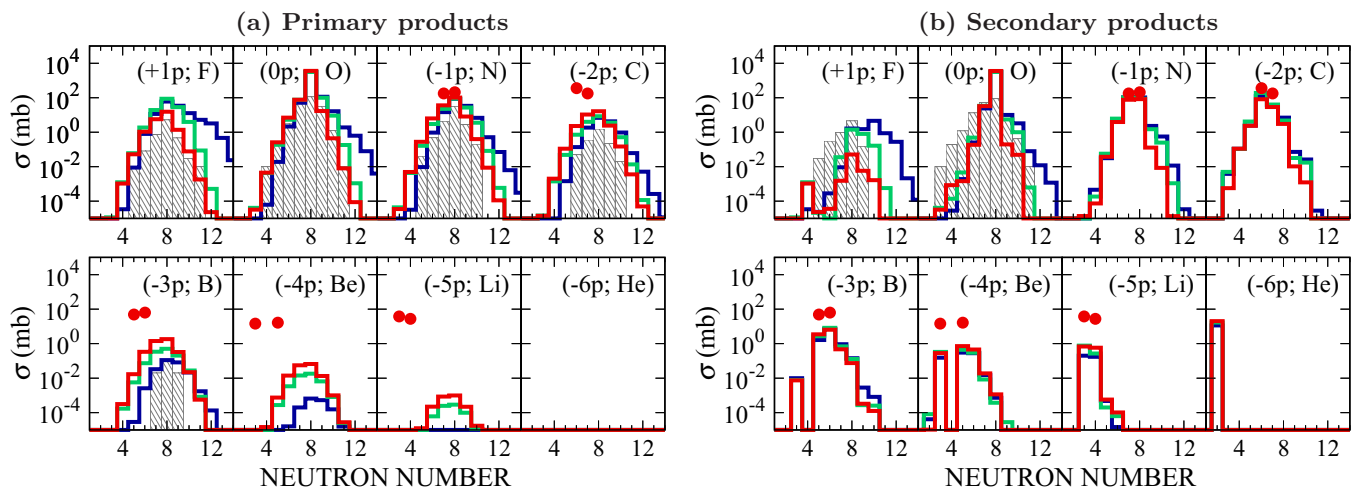


FIG. 11. The  $Q$ -value- and angle-integrated isotope production cross sections for various proton-transfer channels in the  $^{16}\text{O} + ^{27}\text{Al}$  reaction at  $E_{\text{lab}} = 134$  MeV. The change in the number of protons compared with the projectile ( $Z = 8$ ) is indicated as  $(\pm xp; X)$ , where  $X$  stands for the corresponding element. Red filled circles show the experimental data. The results of TDHF(+GEMINI) calculations are shown by histograms. Calculated results for primary (secondary) products are shown in the left (right) figure. GRAZING results [90] are also shown by gray shaded histograms for comparison.

panel, the isotope distribution for a different proton-transfer channel ( $\pm xp$ ) is shown. Unlike in our earlier studies with heavy targets [50], there is no significant decrease in the cross section with the increase of the number of transferred nucleons, probably indicating a different production mechanism for the present light system at this incident energy.

In the TDHF approach, the usage of the particle-number projection method [91] allows us to evaluate production cross sections for primary reaction products before secondary de-excitation processes from the TDHF wave functions [61]. The results of the TDHF calculations are shown in Fig. 11(a) by histograms. Red, green, and blue lines, like before, correspond to the results associated with the shrinking  $x$ ,  $y$ , and  $z$  cases, respectively. Since a proper averaging over the orientations requires a vast computational effort, here we show contributions from each initial orientation examined. For comparison, results of a widely used semiclassical model GRAZING [92] are also shown by gray shaded histograms, although the use of GRAZING may not be suitable for collisions between such light nuclei and at such high incident energy.

From Fig. 11(a), we find a significant discrepancy between the measured cross sections and the TDHF results. Namely, TDHF substantially underestimates the measured cross sections, especially for reaction channels ( $-xp$ ) ( $x \geq 2$ ). Moreover, the experimental data indicate that the peak position of the cross sections should be shifted toward the less neutron-number side for those processes. The discrepancies are very similar to those observed for heavier systems [48,61,64]. For the six-proton stripping reaction ( $-6p$ ), the calculated cross section is negligibly small (below  $10^{-5}$  mb) and cannot be seen in the figure with the present scale settings.

As we have learned from the study of the TKEL spectra that the primary reaction products are highly excited, secondary de-excitation processes via light-particle emissions may substantially alter the final yields of the isotope distributions. A recently developed method, TDHF+GEMINI [48], enables the evaluation of production cross sections for secondary reaction products. In the present work, the TDHF+GEMINI calculations have also been performed and the results are shown in Fig. 11(b). In the calculations, average excitation energy and angular momentum were utilized as detailed in Ref. [48]. We note that the ingredients of the statistical model have been parametrized and determined so as to allow a good systematic description of the evaporation spectra for the entire mass region. Detailed discussions on various modifications and fine-tuning of the model parameters that were implemented in the GEMINI++ code can be found in Refs. [93,94]. Nevertheless, one should keep in mind that the results may be still dependent on the details of the model parameters. Since fine-tuning of those parameters is going beyond the scope of this work, however, we utilize the default parameter setting for the GEMINI++ calculations.

From Fig. 11(b), we find that the inclusion of secondary de-excitation processes significantly affects the isotope distributions. The orientation dependence is almost washed out for the proton-stripping channels ( $-xp$ ) after the inclusion of de-excitation effects. The absolute value of the cross sections for the ( $-1p$ ) and ( $-2p$ ) reactions reasonably agrees with

the experimental data. For other channels, ( $-3p$ ), ( $-4p$ ), and ( $-5p$ ), a significant improvement of the agreement between the TDHF+GEMINI calculations and the experimental data is observed and the overall trend, i.e., the location of the peaks, nicely coincides with the experimental data. However, the theory still underestimates the absolute value of measured cross sections for these reactions as was observed also for heavier systems [48]. We note that owing to the usage of the GEMINI++ de-excitation model, the dip for  $^8\text{Be}$  production that decays into two  $\alpha$  particles is correctly reproduced. In addition, TDHF+GEMINI provides substantial cross sections also for  $^4\text{He}$  production (corresponding to the  $\alpha$  emissions) which can be seen as a prominent single peak in the ( $-6p$ ; He) panel; however, no experimental cross sections are available for comparison. We note that the GRAZING results were obtained for limited reaction channels: It was unable to provide cross sections in many of the proton-stripping channels ( $-xp$ ), which indicates that the model may not be suitable to apply to such a light system at energies substantially above the Coulomb barrier.

To examine further, we have considered two types of division of excitation energy of the fragments, (i) thermal division and (ii) equal division. For the case of the thermal division (i), total excitation energy is shared as it is proportional to the fragment masses, while in the equal division case (ii) the excitation energy is equally shared between two fragments. The results presented in Fig. 11(b) actually correspond to the case of the equal division. By switching from the case (i) to (ii), an increase in the magnitude of the production cross sections for ( $-xp$ ) ( $x \geq 3$ ) reaction channels was observed, as expected (the equal division gives higher excitation energy to the PLFs and thus larger evaporation effects). As this gives a better agreement with the experimental cross sections, some underestimation of evaporation effects within TDHF+GEMINI might be the cause for observed discrepancy between the calculation and measurement, as discussed in Ref. [48].

Lastly, it is important to note that the observed agreement between the TDHF+GEMINI calculations and the experimental data is noteworthy, especially because no particular effort was paid to reproduce the measurements. The present results indicate that the deep-inelastic multinucleon transfer processes followed by light-particle emissions may be the primary production mechanism for the proton-stripping processes in the  $^{16}\text{O} + ^{27}\text{Al}$  reaction at  $E_{\text{lab}} = 134$  MeV.

## V. SUMMARY AND CONCLUSIONS

Deep-inelastic multinucleon transfer processes in the  $^{16}\text{O} + ^{27}\text{Al}$  reaction at  $E_{\text{lab}} = 134$  MeV have been investigated both experimentally and theoretically. The differential cross sections and TKEL distributions for various PLFs have been measured. The TKEL up to about 70 MeV is observed, which indicates the deep-inelastic character of the reaction. The measured angular distributions are forward-peaked and decrease exponentially as the scattering angle increases. The observed behavior supports a picture of a dinuclear system formation and its subsequent decays, similar to quasifission dynamics routinely observed in much heavier systems.

For a deeper understanding of the reaction dynamics, we have carried out a detailed theoretical analysis based on the TDHF theory. From the results, we have found that the global features of the reaction, such as TKEL and the scattering angle, do not depend much on orientations of the deformed  $^{27}\text{Al}$ . On the other hand, the sticking time and the fragment masses show noticeable orientation dependence. In an impact parameter region very close to the fusion threshold, we have found orbiting-type dynamics, where the composite dinuclear system rotates more than  $360^\circ$  in the reaction plane. Depending on initial orientations, we observed generation of mass symmetric fragments after a relatively long sticking time ( $\gtrsim 4$  zs). This observation suggests that a significant contribution of deep-inelastic collisions may be present in the symmetric fusion-fission-like reaction products at this incident energy.

The isotope production cross sections obtained from the measurement and those from the TDHF calculations have been compared. By applying a recently developed method, TDHF+GEMINI [48], production cross sections for secondary products were evaluated. From the comparison, we have found a reasonable agreement between the experimental and theoretical cross sections, especially peak positions of the isotope distributions. The agreement indicates that the deep-inelastic multinucleon transfer followed by light-particle emissions is the primary reaction mechanism in the present case.

In conclusion, the present results suggest that even with a “light+light” system at energies well above the Coulomb barrier we can study a rich many-body reaction mechanism that nicely mimics the one observed in heavy systems, e.g., dinuclear system formation, multinucleon exchanges, energy dissipation, as well as mass equilibration processes. It would be promising to continue this experimental program along with the TDHF analysis to further develop our understanding of the underlying mechanism in low-energy heavy-ion reactions.

#### ACKNOWLEDGMENTS

The authors wish to thank the operation staff of the BARC-TIFR Pelletron-Linac facility, Mumbai, for the excellent support during the experiment. One of the authors (B.J.R.) is thankful to Sangita Hazarika and Srimita Saha, students from Gauhati University, for their interest and involvement in the initial stages of the data analysis. One of the authors (K.S.) acknowledges support of Polish National Science Centre (NCN) Grant Decision No. DEC-2013/08/A/ST3/00708. This research work used computational resources of the HPCI system (HITACHI SR16000/M1) provided by Information Initiative Center (IIC), Hokkaido University, through the HPCI System Research Projects (Project ID No. hp160062 and No. hp170007).

- 
- [1] R. Bass, *Nuclear Reactions with Heavy Ions* (Springer-Verlag, NY, 1980), pp. 213–282.
- [2] C. E. Anderson, W. J. Knox, A. R. Quinton, and G. R. Bach, *Phys. Rev. Lett.* **3**, 557 (1959).
- [3] J. W. Harris, T. M. Cormier, D. F. Geesaman, L. L. Lee, Jr., R. L. McGrath, and J. P. Wurm, *Phys. Rev. Lett.* **38**, 1460 (1977).
- [4] M. B. Tsang, W. G. Lynch, R. J. Puigh, R. Vandenbosch, and A. G. Seamster, *Phys. Rev. C* **23**, 1560 (1981).
- [5] M. Sasagase, M. Sato, S. Hanashima, K. Furuno, Y. Nagashima, Y. Tagishi, S. M. Lee, and T. Mikumo, *Phys. Rev. C* **27**, 2630 (1983).
- [6] S. J. Padalino and L. C. Dennis, *Phys. Rev. C* **31**, 1794 (1985).
- [7] S. J. Padalino, R. A. Parker, and L. C. Dennis, *Phys. Rev. C* **33**, 1805 (1986).
- [8] N. C. Filho, M. M. Coimbra, N. Added, R. M. dos Anjos, L. Fante, Jr., M. C. S. Figueira, V. Guimares, E. M. Szanto, A. S. de Toledo, and O. Civitarese, *Phys. Rev. C* **40**, 91 (1989).
- [9] S. J. Padalino, M. A. Putnam, J. A. Constable, T. G. De Clerck, L. C. Dennis, R. Zingarelli, R. Kline, and K. Sartor, *Phys. Rev. C* **41**, 594 (1990).
- [10] N. Added, R. M. D. Anjos, N. Carlin, L. Fante, M. C. S. Figueira, R. Matheus, E. M. S., A. Szanto de Toledo, M. S. Hussein, C. A. Bertulani, and L. F. Canto, *Nucl. Phys. A* **540**, 328 (1992).
- [11] L. Kowalski, J. C. Jodogne, and J. M. Miller, *Phys. Rev.* **169**, 894 (1968).
- [12] J. Dauk, K. P. Lieb, and A. M. Kleinfeld, *Nucl. Phys. A* **241**, 170 (1975).
- [13] R. L. Kozub, N. H. Lu, J. M. Miller, D. Logan, T. W. Debiak, and L. Kowalski, *Phys. Rev. C* **11**, 1497 (1975).
- [14] B. B. Back, R. R. Betts, C. Gaarde, J. S. Larsen, E. Michelsen, and K.-H. Tai, *Nucl. Phys. A* **285**, 317 (1977).
- [15] Y. Eisen, I. Tserruya, Y. Eyal, Z. Fraenkel, and M. Hillman, *Nucl. Phys. A* **291**, 459 (1977).
- [16] R. Rascher, W. F. J. Müller, and K. P. Lieb, *Phys. Rev. C* **20**, 1028 (1979).
- [17] S. M. Lee, Y. Higashi, Y. Nagashima, S. Hanashima, M. Sato, H. Yamaguchi, M. Yamanouchi, and T. Matsuse, *Phys. Lett. B* **98**, 418 (1981).
- [18] H. Ikezoe, N. Shikazono, Y. Tomita, K. Ideno, Y. Sugiyama, and E. Takekoshi, *Nucl. Phys. A* **444**, 349 (1985).
- [19] I. M. Ladenbauer-Bellis, I. L. Preiss, and C. E. Anderson, *Phys. Rev.* **125**, 606 (1962); **129**, 2835(E) (1963).
- [20] G. F. Gridnev, V. V. Volkov, and J. Wilczynski, *Nucl. Phys. A* **142**, 385 (1970).
- [21] F. Pühlhofer and R. M. Diamond, *Nucl. Phys. A* **191**, 561 (1972).
- [22] T. M. Cormier, A. J. Lazzarini, M. A. Neuhausen, A. Sperduto, K. Van Bibber, F. Videbaek, G. Young, E. B. Blum, L. Herreid, and W. Thoms, *Phys. Rev. C* **13**, 682 (1976).
- [23] T. Mikumo, M. Sasagase, M. Sato, T. Ooi, Y. Higashi, Y. Nagashima, and M. Yamanouchi, *Phys. Rev. C* **21**, 620 (1980).
- [24] D. Shapira, J. L. C. Ford, Jr., J. G. del Campo, and P. H. Stelson, *Phys. Rev. C* **21**, 1824 (1980).
- [25] S. L. Tabor, L. C. Dennis, K. W. Kemper, J. D. Fox, K. Abdo, G. Neuschaefer, D. G. Kovar, and H. Ernst, *Phys. Rev. C* **24**, 960 (1981).
- [26] G. R. Young, K. A. Van Bibber, A. J. Lazzarini, S. G. Steadman, and F. Videbæk, *Phys. Rev. C* **25**, 1304 (1982).
- [27] M. Sato, M. Sasagase, Y. Nagashima, J. Schimizu, T. Nakagawa, Y. Fukuchi, and T. Mikumo, *Phys. Rev. C* **27**, 2621 (1983).
- [28] M. E. Brandan, A. Menchace-Rocha, A. S. de Toledo, N. C. Filho, E. M. Szanto, and M. M. Coimbra, *J. Phys. G: Nucl. Part. Phys.* **12**, 391 (1986).

- [29] W. Shen, Y. Zhu, W. Zhan, Z. Guo, S. Yin, W. Qiao, and X. Yin, *Nucl. Phys. A* **472**, 358 (1987).
- [30] C. Bhattacharya, K. Mullick, S. Bhattacharya, K. Krishan, T. Bhattacharjee, P. Das, S. R. Banerjee, D. N. Basu, A. Ray, S. K. Basu, and M. B. Chatterjee, *Phys. Rev. C* **66**, 047601 (2002).
- [31] C. Bhattacharya, S. Bhattacharya, T. Bhattacharjee, A. Dey, S. Kundu, S. R. Banerjee, P. Das, S. K. Basu, and K. Krishan, *Phys. Rev. C* **69**, 024607 (2004).
- [32] R. K. Choudhury, D. M. Nadkarni, V. S. Ambekar, B. V. Dinesh, A. Saxena, M. S. Sawant, D. C. Biswas, and L. M. Pant, *Pramana* **44**, 177 (1995).
- [33] M. Cavallaro, F. Cappuzzello, D. Carbone, A. Cunsolo, A. Foti, R. Linares, D. Pereira, J. R. B. Oliveira, P. R. S. Gomes, J. Lubian, and R. Chen, *Nucl. Instrum. Methods A* **648**, 46 (2011).
- [34] D. Pereira, R. Linares, J. R. B. Oliveira, J. Lubian, L. C. Chamon, P. R. S. Gomes, A. Cunsolo, F. Cappuzzello, M. Cavallaro, D. Carbone, and A. Foti, *Phys. Lett. B* **710**, 426 (2012).
- [35] J. R. B. Oliveira, F. Cappuzzello, L. C. Chamon, D. Pereira, C. Agodi, M. Bondi, D. Carbone, M. Cavallaro, A. Cunsolo, M. De Napoli *et al.*, *J. Phys. G: Nucl. Part. Phys.* **40**, 105101 (2013).
- [36] F. Cappuzzello, D. Nicolosi, R. Linares, J. R. B. Oliveira, J. Lubian, C. Agodi, D. Carbone, M. Cavallaro, P. N. de Faria, A. Foti, and M. R. D. Rodrigues, *Eur. Phys. J. A* **52**, 169 (2016).
- [37] D. Pereira, J. Lubian, J. R. B. Oliveira, D. P. de Sousa, and L. C. Chamon, *Phys. Lett. B* **670**, 330 (2009).
- [38] J. Galin, D. Guerreau, M. Lefort, J. Peter, X. Tarrago, and R. Basile, *Nucl. Phys. A* **159**, 461 (1970).
- [39] A. G. Artukh, G. F. Gridnev, V. L. Mikheev, V. V. Volkov, and J. Wilczyński, *Nucl. Phys. A* **215**, 91 (1973).
- [40] R. Albrecht, W. Dunnweber, G. Graw, H. Ho, S. G. Steadman, and J. P. Wurm, *Phys. Rev. Lett.* **34**, 1400 (1975).
- [41] V. V. Volkov, *Phys. Rep.* **44**, 93 (1978).
- [42] R. Broda, B. Fornal, W. Krolas, T. Pawlat, J. Wrzesinski, D. Bazzacco, G. de Angelis, S. Lunardi, and C. Rossi Alvarez, *Eur. Phys. J. A* **20**, 145 (2003).
- [43] E. M. Kozulin, E. Vardaci, G. N. Knyazheva, A. A. Bogachev, S. N. Dmitriev, I. M. Itkis, M. G. Itkis, A. G. Knyazev, T. A. Loktev, K. V. Novikov *et al.*, *Phys. Rev. C* **86**, 044611 (2012).
- [44] J. S. Barrett, W. Loveland, R. Yanez, S. Zhu, A. D. Ayangeakaa, M. P. Carpenter, J. P. Greene, R. V. F. Janssens, T. Lauritsen, E. A. McCutchan *et al.*, *Phys. Rev. C* **91**, 064615 (2015).
- [45] Y. X. Watanabe, Y. H. Kim, S. C. Jeong, Y. Hirayama, N. Imai, H. Ishiyama, H. S. Jung, H. Miyatake, S. Choi, J. S. Song *et al.*, *Phys. Rev. Lett.* **115**, 172503 (2015).
- [46] R. Bass, *Nucl. Phys. A* **231**, 45 (1974).
- [47] R. Bass, *Phys. Rev. Lett.* **39**, 265 (1977).
- [48] K. Sekizawa, *Phys. Rev. C* **96**, 014615 (2017).
- [49] R. J. Charity, *Joint ICTP-AIEA Advanced Workshop on Model Codes for Spallation Reactions*, Report INDC(NDC)-0530 (IAEA, Vienna, 2008), p. 139.
- [50] Sonika, B. J. Roy, A. Parmar, U. K. Pal, H. Kumawat, V. Jha, S. K. Pandit, V. V. Parkar, K. Ramchandran, K. Mahata, A. Pal, S. Santra, A. K. Mohanty, and K. Sekizawa, *Phys. Rev. C* **92**, 024603 (2015).
- [51] I. J. Thompson, *Comput. Phys. Rep.* **7**, 167 (1988) [<http://www.fresco.org.uk>].
- [52] D. Montanari, L. Corradi, S. Szilner, G. Pollarolo, E. Fioretto, A. M. Stefanini, E. Farnea, C. Michelagnoli, G. Montagnoli, F. Scarlassara *et al.*, *EPJ Web Conf.* **63**, 02006 (2013).
- [53] Y. H. Kim, Y. X. Watanabe, Y. Hirayama, N. Imai, H. Ishiyama, S. C. Jeong, H. Miyatake, S. Choi, J. Song, E. Clement *et al.*, *EPJ Web Conf.* **66**, 03044 (2014).
- [54] K. E. Rehm, *Annu. Rev. Nucl. Part. Sci.* **41**, 429 (1991).
- [55] L. Corradi, A. M. Vinodkumar, A. M. Stefanini, E. Fioretto, G. Prete, S. Beghini, G. Montagnoli, F. Scarlassara, G. Pollarolo, F. Cerutti, and Aage Winther, *Phys. Rev. C* **66**, 024606 (2002).
- [56] C. Mayer-Hricke, W. Oelert, A. Kiss, M. Rogge, P. Turek, and S. Wktor, *Nucl. Phys. A* **293**, 189 (1977).
- [57] A. Kiss, C. Mayer-Boricke, M. Rogge, P. Turek, and S. Wktor, *Phys. Rev. Lett.* **37**, 1188 (1976).
- [58] V. Jha, B. J. Roy, A. Chatterjee, and H. Machner, *Euro. Phys. J. A* **19**, 347 (2004).
- [59] J. Galin, *J. Phys. (Paris), Colloq. C5*, **37**, 83 (1976).
- [60] M. Lefort and C. Ngo, *Ann. Phys. (NY)* **3**, 5 (1978).
- [61] K. Sekizawa and K. Yabana, *Phys. Rev. C* **88**, 014614 (2013); **93**, 029902(E) (2016).
- [62] K. Sekizawa and K. Yabana, *Phys. Rev. C* **90**, 064614 (2014).
- [63] K. Sekizawa, Multinucleon transfer reactions and quasifission processes in time-dependent Hartree-Fock theory, Ph.D. thesis, University of Tsukuba, Tsukuba, Japan, 2015 (unpublished).
- [64] K. Sekizawa and K. Yabana, *Phys. Rev. C* **93**, 054616 (2016).
- [65] K. Sekizawa and S. Heinz, *Acta Phys. Pol. B Proc. Suppl.* **10**, 225 (2017).
- [66] K. Sekizawa, *Phys. Rev. C* **96**, 041601(R) (2017).
- [67] J. W. Negele, *Rev. Mod. Phys.* **54**, 913 (1982).
- [68] C. Simenel, *Eur. Phys. J. A* **48**, 152 (2012).
- [69] T. Nakatsukasa, *Prog. Theor. Exp. Phys.* **2012**, 01A207 (2012).
- [70] J. A. Maruhn, P.-G. Reinhard, P. D. Stevenson, and A. S. Umar, *Compt. Phys. Commun.* **185**, 2195 (2014).
- [71] T. Nakatsukasa, K. Matsuyanagi, M. Matsuo, and K. Yabana, *Rev. Mod. Phys.* **88**, 045004 (2016).
- [72] E. Chabanat, P. Bonche, P. Haensel, J. Meyer, and R. Schaeffer, *Nucl. Phys. A* **635**, 231 (1998); **643**, 441 (1998).
- [73] P. Möller, A. J. Sierk, T. Ichikawa, and H. Sagawa, *At. Data Nucl. Data Tables* **109-110**, 1 (2016).
- [74] K. R. S. Devi, A. K. Dhar, and M. R. Strayer, *Phys. Rev. C* **23**, 2062 (1981).
- [75] J. Wilczyński, *Phys. Lett. B* **47**, 484 (1973).
- [76] K. T. R. Davies, V. Maruhn-Rezwani, S. E. Koonin, and J. W. Negele, *Phys. Rev. Lett.* **41**, 632 (1978).
- [77] K. T. R. Davies, K. R. S. Devi, and M. R. Strayer, *Phys. Rev. C* **20**, 1372 (1979).
- [78] K. R. S. Devi, M. R. Strayer, J. M. Irvine, and K. T. R. Davies, *Phys. Rev. C* **23**, 1064 (1981).
- [79] K. T. R. Davies and S. E. Koonin, *Phys. Rev. C* **23**, 2042 (1981); **24**, 1820(E) (1981).
- [80] A. K. Dhar and A. C. Merchant, *Phys. Rev. C* **29**, 1331 (1984).
- [81] E. Williams, K. Sekizawa, D. J. Hinde, C. Simenel, M. Dasgupta, I. P. Carter, K. J. Cook, D. Y. Jeung, S. D. McNeil, C. S. Palshetkar *et al.*, *Phys. Rev. Lett.* **120**, 022501 (2018).
- [82] V. E. Viola, K. Kwiatkowski, and M. Walker, *Phys. Rev. C* **31**, 1550 (1985).
- [83] D. J. Hinde, J. R. Leigh, J. J. M. Borkhorst, J. O. Newton, R. L. Walsh, and J. W. Boldeman, *Nucl. Phys. A* **472**, 318 (1987).
- [84] D. J. Hinde, D. Hilscher, H. Rossner, B. Gebauer, M. Lehmann, and M. Wilpert, *Phys. Rev. C* **45**, 1229 (1992).

- [85] R. du Rietz, D. J. Hinde, M. Dasgupta, R. G. Thomas, L. R. Gasques, M. Evers, N. Lobanov, and A. Wakhle, *Phys. Rev. Lett.* **106**, 052701 (2011).
- [86] R. du Rietz, E. Williams, D. J. Hinde, M. Dasgupta, M. Evers, C. J. Lin, D. H. Luong, C. Simenel, and A. Wakhle, *Phys. Rev. C* **88**, 054618 (2013).
- [87] A. Wakhle, C. Simenel, D. J. Hinde, M. Dasgupta, M. Evers, D. H. Luong, R. du Rietz, and E. Williams, *Phys. Rev. Lett.* **113**, 182502 (2014).
- [88] E. Prasad, D. J. Hinde, E. Williams, M. Dasgupta, I. P. Carter, K. J. Cook, D. Y. Jeung, D. H. Luong, C. S. Palshetkar, D. C. Rafferty *et al.*, *Phys. Rev. C* **96**, 034608 (2017).
- [89] See Supplemental Material at <http://link.aps.org/supplemental/10.1103/PhysRevC.97.034603> for movies of the reactions for typical initial conditions.
- [90] A. Winther, program GRAZING\_9, <http://personalpages.to.infn.it/~nanni/grazing/>; the default parameter set was used for the calculation.
- [91] C. Simenel, *Phys. Rev. Lett.* **105**, 192701 (2010).
- [92] A. Winther, *Nucl. Phys. A* **572**, 191 (1994); **594**, 203 (1995).
- [93] R. J. Charity, *Phys. Rev. C* **82**, 014610 (2010).
- [94] D. Mancusi, R. J. Charity, and J. Cugnon, *Phys. Rev. C* **82**, 044610 (2010).